



저작자표시-비영리-변경금지 2.0 대한민국

이용자는 아래의 조건을 따르는 경우에 한하여 자유롭게

- 이 저작물을 복제, 배포, 전송, 전시, 공연 및 방송할 수 있습니다.

다음과 같은 조건을 따라야 합니다:



저작자표시. 귀하는 원저작자를 표시하여야 합니다.



비영리. 귀하는 이 저작물을 영리 목적으로 이용할 수 없습니다.



변경금지. 귀하는 이 저작물을 개작, 변형 또는 가공할 수 없습니다.

- 귀하는, 이 저작물의 재이용이나 배포의 경우, 이 저작물에 적용된 이용허락조건을 명확하게 나타내어야 합니다.
- 저작권자로부터 별도의 허가를 받으면 이러한 조건들은 적용되지 않습니다.

저작권법에 따른 이용자의 권리는 위의 내용에 의하여 영향을 받지 않습니다.

이것은 [이용허락규약\(Legal Code\)](#)을 이해하기 쉽게 요약한 것입니다.

[Disclaimer](#)

Chapter 1. Introduction

1.1 Neural tissue engineering

Tissue engineering (TE), an emerging solution for tissue and organ failure, is the technique to repair or replace damaged tissues with a composite of cells, scaffolds and suitable biomolecules [1–5]. The cells seeded on scaffolds are grown to desired tissues and ultimately implanted at damaged sites of organs (**Figure 1**). This technique has been applied to bone, blood vessels, cartilage, liver, muscle, skin and even nerve damage treatments [6–11]. In particular, neural tissue engineering is a precious treatment in neurological damage as nerve cells and tissues hardly regenerate on their own after nerve injury has occurred [11]. For nerve regeneration, cell and biomolecule delivery therapies have been investigated for a long time. However, direct cell injection has a problem of the inhospitable environment around the injury site, which lead to cell death and low efficacy. Direct biomolecule injection has issues about off-target distribution, so requires encapsulation strategies for controlled delivery. Thus, scaffold-based treatment in combination with above treatments, that is a tissue engineering, is an attractive alternative because it can enhance both cell survival and local delivery of biomolecules [5].

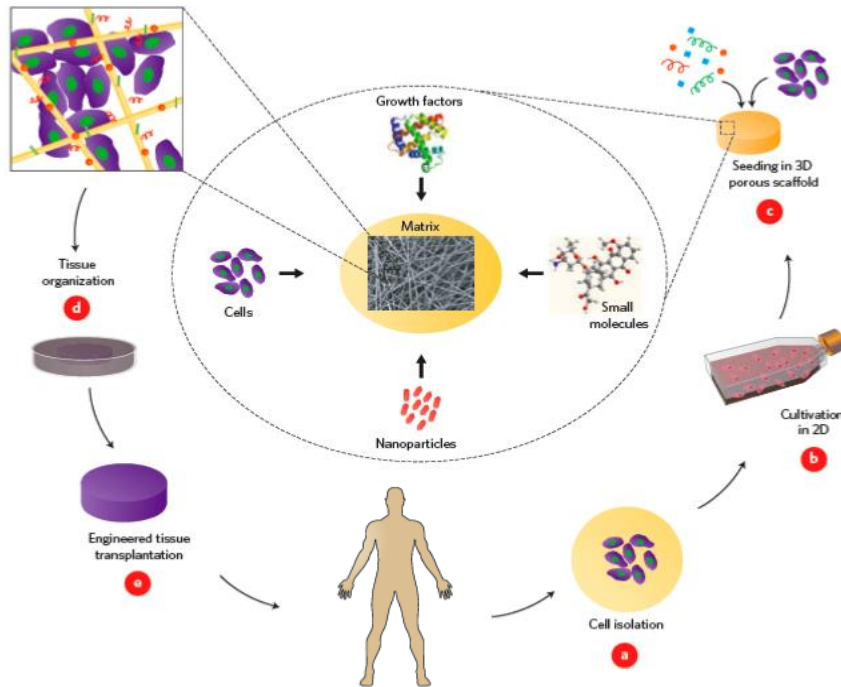


Figure 1. An example of a tissue engineering concept that involves seeding cells within porous biomaterial scaffolds. (a) Cells are isolated from the patient and cultivated (b) *in vitro* on two-dimensional surfaces for efficient expansion. (c) Next, the cells are seeded in porous scaffolds together with growth factors, small molecules, and micro- and/or nanoparticles. The scaffolds serve as a mechanical support and a shape-determining material, and their porous nature provides high mass transfer and waste removal. (d) The cell constructs are further cultivated in bioreactors to provide optimal conditions for organization into a functioning tissue. (e) Once a functioning tissue has been successfully engineered, the construct is transplanted on the defect to restore function [3].

1.1.1 Requirements of scaffolds for tissue engineering

A critical point for successful implantation of engineered tissue *in vivo* is the production of the appropriate scaffold which supports cells as well as promotes cell activities such as cell growth, proliferation, and differentiation. The engineering scaffolds share considerable factors for proper choice of scaffold along the specific applications. In respect of physical properties of scaffolds, suitable pore volume and pore size distribution are needed to provide living space for cells and route for cell migration and nutrient delivery. The optimum pore size depends on the type of cells and tissue. In previous research, it has been demonstrated that the optimal pore size or range of scaffold was 5 μm for neovascularization, ~ 10 μm for fibroblast growth, 40 to 100 μm for osteoid ingrowth, 250 to 500 μm for chondrocyte's proliferation, and > 250 μm for vascularization [12–14]. Regarding nerve cells, Zander *et al.* [15] reported that PC 12 cells prefer 6 to 10 μm of pore size for cell infiltration and growth. Furthermore, mechanical strength of scaffold plays an important role in supporting cells and protecting against from external physical impact. In addition, appropriate mechanical properties improve cell functions by giving correct stress to cells. The proper value of scaffold mechanical strength was generally known to accord with the elasticity of desired tissue or organs. Soft scaffolds that mimic brain elasticity (0.1–1 kPa) are neurogenic, stiffer

scaffolds that mimic muscle elasticity (8–17 kPa) are myogenic, and relatively rigid scaffold mimic collagenous bone (25–40 kPa) are osteogenic [16]. In the case of neurons, Georges *et al.* demonstrated that soft substrate was required for effective neuronal cell attachment and growth, but neurite extension was not significantly affected by substrate stiffness [17].

The second issue is chemical properties of scaffolds. The scaffold should be biocompatible for *in-vivo* implantation and further possessed of surface chemistry activating cell functions. There are two ends at membrane proteins, N-terminus with a free amine group (-NH₂) and C-terminus with an unbound carboxyl group (-COOH). These two terminus are critical to enable functions of specialized proteins *via* interaction with other molecules. As expected, substrates with functional group having potential to bond with N-terminus or C-terminus could activate cells effectively. Previous researches have reported that N-containing substrates enhance cell adhesion and carboxyl group has a decisive effect on neurite formation [18, 19]. In addition, functional groups on substrate can be coupled with bioactive molecules, such as poly-lysine, gelatin, collagen and some growth factors [20, 21].

1.1.2 Signaling pathways for cell activities

Above-mentioned physical and chemical factors can modulate cellular activities by facilitating specific signaling pathways. Mitogen-activated protein kinase (MAPK) families occupy a central position in conversion from external signals to cellular responses. Three different MAPK pathways (ERK, p38 and JNK) have been obviously investigated in mammalian cells (**Figure 2**) [22].

Extracellular signal-regulated kinase (ERK) is the main MAPK involved in activating cell differentiation and its family has the most ubiquitous signaling mechanisms. In the response to neurotrophins, the ERK pathway starts at Trk receptors which give a tight binding site for a neurotrophin. There are three common Trk receptors, TrkA, TrkB and TrkC. Nerve growth factor (NGF) specifically binds to a TrkA receptor. The stimulation of TrkA provokes the activation of the raf kinase, which is followed by phosphorylation of MEK1/2 kinase. Phosphorylated MEK1/2 then results in activation of ERK1/2 kinase that can phosphorylate numerous cellular proteins and also penetrate into nucleus to act on transcription factors [22, 23].

The p38 kinase (p38) and c-Jun N-terminal kinase (JNK) are a class of MAPKs that are preferentially responsive to a wide variety of cellular stress including cytokines, UV irradiation, cytotoxic stresses, heat shock and high osmotic shock. An array of kinases such as TAK1, ASK1, MEKK and MLKs have been identified as modulators of the p38 or JNK pathways. TAK1

stimulated by TGF beta and bone morphogenetic proteins (BMPs) activates p38 kinase through MKK3/MKK6. In response to oxidative stress, endoplasmic reticulum stress and influx of calcium, ASK1 phosphorylates greatly MKK3/6 and slightly MKK4, which lead to activation of p38 and JNK pathways, respectively. Among MEKKs, MEKK4 can trigger both p38 and JNK pathways by actuating MKK4/MKK7 and MKK3/MKK6, respectively. The mixed lineage kinase (MLK) family mostly activates the JNK pathway and several MLKs also activate the p38 pathway [24–26].

Furthermore, the level of cytosolic calcium ion is an important factor for MAPK pathways. The increase of cytosolic Ca^{2+} results in the activation of calcium/calmodulin-dependent protein kinases (CaMKs) leading to phosphorylation and activation of ASK1 and a series of proteins from Trk receptor to raf kinase, which are main components of MAPK pathways [26, 27].

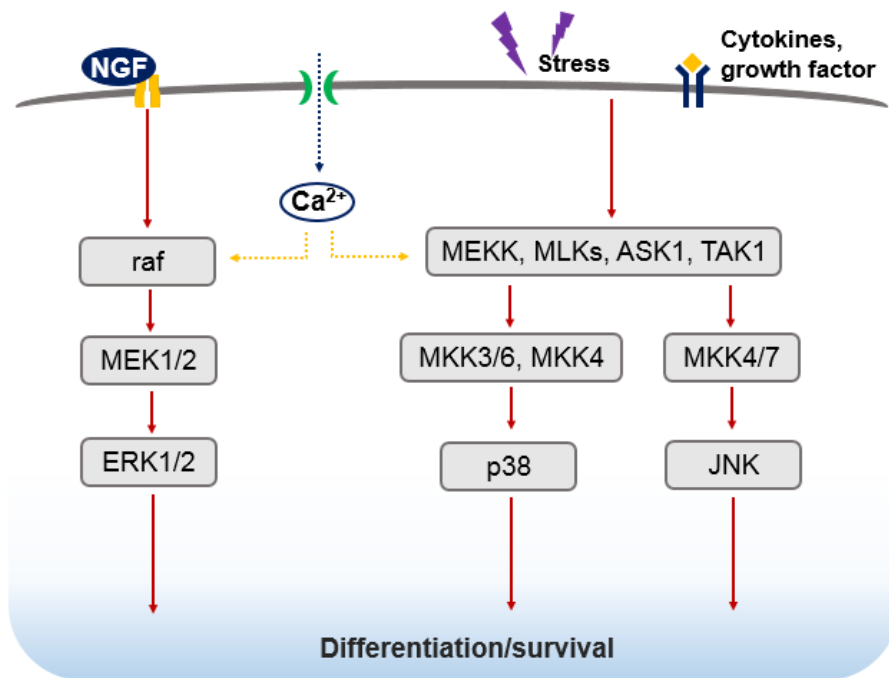


Figure 2. Components of MAPK pathways on differentiation and survival in mammalian cell culture systems.

1.2 Graphene based scaffolds

Graphene, a sp^2 -hybridized carbon monolayer, has received great attention due to their superior properties such as large surface area ($\sim 2630 \text{ m}^2\text{g}^{-1}$), remarkable mechanical strength (Young's modulus of $\sim 1 \text{ TPa}$), electrical (charge carrier mobility of $\sim 200000 \text{ cm}^2\text{V}^{-1}\text{s}^{-1}$) and thermal ($\sim 500 \text{ Wm}^{-1}\text{K}^{-1}$) conductivities, and unique optical properties [28–30]. Also, graphene and its derivatives can be further functionalized by both covalent and non-covalent bonding to surpass the chemistry of pristine graphene [31]. In addition to such fascinating properties, the biocompatibility of graphene is enough to be applied in biomedical fields including drug delivery, bio-imaging, bio-sensor and tissue engineering [32, 33]. Among them, graphene-based scaffold is emerging as a hot issue for tissue engineering. At first, researchers paid attention to the stiffness of graphene, which supplemented the mechanical drawback of traditional scaffold materials like collagen, chitosan, alginate and PVA. At that time, they also recognized additional benefits from graphene not only enhancing attachment of proteins and cells on a substrate but also accelerating proliferation and differentiation of cells [34–36]. These results lead people to the investigation of graphene-based scaffold with 2D and 3D structures. Concerning 2D structures, graphene sheets were generally coated onto a glass and other 2D films or agglomerated together to form a film. Lee *et al.* and Chen *et al.* demonstrated that the surface chemistry of graphene family affected cell

functions using graphene or graphene oxide coated PDMS and graphene film, respectively [37, 38]. Beyond two dimension, 3D scaffolds are highly required for the success of clinical applications. In general, 3D structures of graphene have been fabricated by the CVD method and the exfoliation-reduction method. Concerning neural cells, Ning Li fabricated the CVD-grown 3D graphene foam with porous structure using nickel foam template and applied it for the first time to neural stem cell (NSC) culture. The 3D graphene foam not only supported the growth of NSC but also enhanced the proliferation and the differentiation towards neurons [39]. Actually, the hydrogel foams of graphene (GO and RGO hydrogels) are better than the CVD-grown graphene foam in terms of stiffness suited to neuron, but there have been few researches on the applications of such foams [40].

Despite progressive developments in effects of graphene-based scaffolds in neural cell, there is a lack of understanding how graphene work to enhance neural functions. Among complex neural signaling pathways, Ning Li demonstrated that neurite growth and development were affected by graphene through growth associated protein-43 pathway in 2011 [41]. Recently, Shreyas Shah investigated several proteins known as key mediators for integrin-ECM signaling pathway (FAK, Akt, ILK and Fyn) and concluded that graphene would promote oligodendrocyte differentiation through interactions with integrins [42].

1.3 Objective of this study

Herein, nanoparticles-embedded 3D RGO scaffolds were applied to a neural cell culture. Silica/titania hollow nanoparticle ($\text{SiO}_2/\text{TiO}_2$ HNP) and barium doped silica/titania hollow nanoparticle ($\text{Ba-SiO}_2/\text{TiO}_2$ HNP) were inserted into RGO hydrogel during the reduction process to assign additional bioactive effects to RGO hydrogel. First, the suitability of physical and chemical properties of fabricated scaffolds were confirmed. The pore size distribution and stiffness were suited to PC12 cell, well-known model cell for neuron. All the hydrogels were non-toxic to cells and even improved cell proliferation. Due to the scaffold softness and surface functional groups, cell adhesion also increased. Neurite growth were enhanced in order of Ba-HNP-RGO hydrogel > HNP-RGO hydrogel > RGO hydrogel. As mentioned above, the research about how graphene work to cell activities was not yet greatly revealed. Considering the fact that ROS level, an indicator of oxidative stress, was coincidence with the result of neurite growth, the MAPK pathways known to be affected by cellular stress were examined to investigate the effect of RGO on signaling pathways. This research may provide improved understanding about graphene based scaffold for neuron.

Chapter 2. Experimental

2.1 Materials

Tetraethyl orthosilicate (TEOS, 98%), titanium isopropoxide (TTIP, 97%), barium hydroxide ($\text{Ba}(\text{OH})_2$, ~95%), L-ascorbic acid (Vitamin C, 99%) and natural graphite were purchased from Sigma-Aldrich Chemical Co. Potassium permanganate (KMnO_4 , 99.3%) and phosphorous pentoxide (P_2O_5 , extra pure) were supplied from the Junsei Chemical Co. Potassium persulfate ($\text{K}_2\text{S}_2\text{O}_8$, 99%) was acquired from the Kanto Chemical Co. Ammonium hydroxide (NH_4OH , 28.0~30.0%), acetonitrile (CH_3CN , 99.5%), absolute ethanol ($\text{C}_2\text{H}_5\text{OH}$, 99.9%), sulfuric acid (H_2SO_4 , 95%), hydrochloric acid (HCl , 35~37%) and hydrogen peroxide (H_2O_2 , 30~35.5%) were purchased from Samchun Chemical. Co. Cell culture medium (RPMI), fetal bovine serum (FBS), horse serum (HS), anti-anti (100X), and additional substances for cell culture and *in vitro* tests were attained from Gibco-by life technologies. Antibodies to pp38, pERK, pJNK, TrkA and goat anti mouse FITC-conjugated secondary antibody were supplied from Santa Cruz Biotechnology, Inc.

2.2 Preparation of silica/titania hollow nanoparticles (HNP and Ba-HNP)

The HNPs were prepared by sonication mediated etching treatment of silica/titania core/shell nanoparticles. First, silica nanoparticles (SiO_2) were formed by the Stöber method. Briefly, 2.9 ml of tetraethyl orthosilicate (TEOS) was dissolved in a mixture of 1.4 ml distilled water, 79 ml absolute ethanol and 3.9 ml ammonia. The resulting solution was reacted for 12 hours at 45 °C and then cooled to 4 °C for the next step. To prepared SiO_2 solution, 3 ml of titanium isopropoxide (TTIP) diluted with 18 ml absolute ethanol and 6 ml acetonitrile was added to form titania shell. After being stirred for 12 hours, the obtained silica/titania core/shell nanoparticles were subsequently converted to HNP and Ba-HNP by etching with ammonia and barium hydroxide solutions for 3 hours under sonication, respectively. The HNPs were washed three times with DI water to remove excessive basic solution.

2.3 Preparation of graphene oxide solution

Graphene oxide (GO) solution was prepared from natural graphite according to the modified Hummer's method [43]. First, 3.0 g of graphite powder was pre-oxidized using potassium persulfate ($\text{K}_2\text{S}_2\text{O}_8$) and

phosphorous pentoxide (P_2O_5) dissolved in sulfuric acid (H_2SO_4) for 5 hours at 80 °C, after which the mixture was diluted with 500 ml DI water and left overnight. After vacuum filtration of the mixture, the residue was left overnight under ambient conditions. In the second step, pre-oxideized graphite powder was poured into concentrated sulfuric acid solution with vigorous stirring. Sequentially, $KMnO_4$ was added carefully into above mixture keeping the temperature below 10 °C in ice bath and then reacted for 2 hours at 35 °C. Then 900 mL DI water was slowly added, keeping the temperature below 50 °C. When the mixture maintained a constant temperature, additional DI water (700 mL) was poured into the mixture. After stirring for another 2 hours, 12 mL of 30% H_2O_2 was injected to finish the reaction. The resulting solution was allowed to stand for 12 h then washed with 10 wt % aqueous HCl solution and DI water in sequence until the pH of solution reached to 7. This graphitic oxide solution was ultra-sonicated for 30 min at 450 W power to exfoliate graphitic oxide into graphene oxide.

2.4 Fabrication of the HNPs embedded reduced graphene oxide (RGO) hydrogel

RGO hydrogel was fabricated by the reduction of GO with ascorbic acid (VC). As-prepared GO solution (0.5 mg mL^{-1}) was mixed with ascorbic acid

with a mass ratio of VC to GO as 10 to 1. After vigorously stirring for 1 hour, the solution was placed in 80 °C oven for 6 hours to obtain 3D RGO hydrogel. After heat treatment, the 3D RGO hydrogel was washed three times with DI water and lyophilized for 48 hours. Similarly, HNP embedded RGO hydrogel and Ba-HNP embedded RGO hydrogel were fabricated by adding HNP and Ba-HNP to the GO/VC mixture with a mass ratio of HNPs to GO as 5 to 1, respectively.

2.5 Instrument of analysis

the HNPs embedded RGO hydrogels characterization: Transmission electron microscope (TEM) images were acquired with a LIBRA 120 (Carl Zeiss, Germany). Atomic force microscope (AFM) images were achieved using Innova AFM (Bruker, USA). Scanning electron microscope (SEM) images were obtained with a JSM-6701F (JEOL, Japan). Atomic percent of the elements (Si, Ti and Ba) were quantified with an INCA energy dispersive X-ray spectrometer (Oxford Instruments Analytical Ltd. UK) linked with SEM. X-ray diffraction (XRD) analyses were conducted with a SmartLab X-ray diffractometer (Rigaku, Japan). X-ray photoelectron spectroscopy (XPS) spectra were observed by a Thermo-VG (Sigma Probe, UK). The pore size of hydrogels was measured using an Autopore-IV-9500 (Micromeritics, USA).

Investigation of differentiation promoting effect and biocompatibility: For *in vitro* experiments, rat pheochromocytoma PC12 cell (American Type Culture Collection, Manassas, VA, USA) were cultured in RPMI medium with 10% horse serum (HS), 5% fetal bovine serum (FBS), and 1% penicillin streptomycin solution. They were raised in a 75T flask at 37 °C in humidified 5% CO₂ atmosphere and passaged at 70%–80% confluence.

To investigate the differentiation promoting effect of scaffolds, PC12 cells were seeded at a density of 2×10^5 cells per well in 24-well plates containing cover glass slips and RGO hydrogels, respectively. A day later, these cells were incubated in a serum-reduced medium (RPMI with 1% HS and 0.5% FBS) and 100 ng mL⁻¹ of nerve growth factor (NGF) and 0.1% bovine serum albumin (BSA) were injected to the medium to induce differentiation. Culture media were changed and supplied with fresh NGF and BSA every day. The neuronal differentiation of PC12 cells on the glass and on the hydrogels was evaluated by specifically staining β -tubulin with Alexa Fluor 488 Mouse anti- β -Tubulin, Class III (BD Bioscience). After incubation for 1-3 days, differentiated PC12 cells were fixed with 4% paraformaldehyde (PFA) for 10 min, permeabilized with 0.5% Triton X-100 for 5 min, and blocked with 0.1% BSA for 15 min. Then, these cells were incubated with anti- β -tubulin overnight at 37 °C. After rinsing with 0.1M PBS and staining nuclei with DAPI, fluorescent images was achieved by a Confocal Microscope SP8 X (Leica, Germany) using Diode 405

and argon laser.

Furthermore, the influence of each scaffold on the signaling pathway of the cells was examined by protein expression analysis. As described above, differentiated PC12 cells were fixed with 4% PFA for 20 min, permeabilized with 0.1% Triton X-100 for 15 min, and blocked with 0.1M PBS solution consisting of 10% FBS and 0.03% 1 M NaN₃ for 30 min. Then, the cells were treated with specific primary antibodies against signaling pathway-related proteins (pp38, pERK1/2, pJNK and TrkA) for 1 hour, respectively. The cells were stained with secondary antibody (FITC conjugated goat anti mouse) for another 1 hour, and analyzed by FACS Calibur flow cytometer (BD Biosciences, USA)

To evaluate the biocompatibility of scaffolds, cell viability was assessed using Cell-Titer glo luminescent assay (Promega, Madison, WI, USA). This assay determines the number of viable cells based on the quantity of ATP from live cells. Briefly, cultured cells were treated with D-luciferin and luciferase which changed D-luciferin to luminescent oxyluciferin by consuming ATP, and then the luminescence was measured by Victor3 Multilabel Reader (PerkinElmer, Boston, MA, USA) at 595 nm emission. Likewise, the extent of reactive oxygen species (ROS) formation was quantified by a fluorometric microplate assay. 2',7'-Dichlorofluorescein diacetate (Invitrogen, Grand Island, NY, USA) was injected into the cultures and turned to fluorescent 2',7'-

dichlorofluorescein upon oxidation by ROS. Fluorescent intensity was detected by Victor3 Multilabel Reader at 485 nm excitation and 535 nm emission. To visually confirm the cell viability, fluorescent microscopy analysis was performed using Live/Dead cell imaging kit 488/570 (Molecular probes by life technologies). Cells were seeded at a density of 5×10^6 cells per well in 8-well plates at which each well included cover slip and the RGO hydrogels, respectively. After 24 hours of incubation, live and dead cells were stained differently with green and red dyes. Stained cells were observed by Confocal Microscope SP8 X (Leica, Germany) using argon and DPSS561 laser.

Chapter 3. Results and discussion

3.1 Fabrication of RGO hydrogel scaffolds

The fabrication processes for RGO hydrogel scaffolds and their further application as supports for PC12 cells are illustrated in **Figure 3**. In this work, graphene oxide sheets were synthesized *via* slightly modified Hummer's method (**Figure 3a**) [43]. Through several steps of oxidation, graphite sheets with various oxygen functional groups moved apart from each other. The graphene oxide (GO) sheets were finally obtained after ultra-sonication process. The GO sheets were dissolved in water to prepare 0.5 mg mL⁻¹ of GO solution. Different types of HNPs (HNP and Ba-HNP) were produced by sonication mediated etching redeposition (SMER) process of silica/titania core/shell nanoparticles (**Figure 3b**). Silica nanoparticles prepared by stöber method were coated with TiO₂ shell *via* TTIP addition. Subsequently, the resulting core/shell nanoparticles were etched in a basic solution with sonication. Silica in the boundary of core and shell was dissolved in a basic solution in accord with sol-gel process, while titania was hardly dissolved in the same condition [44]. This selective etching created void spaces between silica core and titania shell, at

which sonic irradiation produces intense local energy by collapsing bubble and forming acoustic cavitation. By means of extra energy by sonication, the silica core part was wholly etched and some of etched silica were condensed and redeposited near the titania shell because of Ostwald ripening [45]. Consequently, hollow nanoparticles (HNPs) with silica/titania composite was obtained by this SMER method. In regard of barium hydroxide as etchant instead of ammonia, barium ion also participated in the formation of metal oxides and then settled in the form of BaSiO_3 or BaTiO_3 , resulting in Ba-doped HNP termed Ba-HNP.

After fabricating GO and HNPs, graphene based hydrogel scaffolds were fabricated by employing prepared GO and HNPs as building blocks. The GO solution was mixed with or without HNPs (mass ratio of GO: HNPs = 1:5) and reduced by L-ascorbic acid (VC, mass ratio of GO: VC = 1:10), that is a mild and environmental-friendly reducing agent, under 80 °C atmosphere. According to reduction process, reduced graphene oxide (RGO) sheets were restacked and finally formed 3D structures with porous network. The resulting three different types of hydrogels, denominated as RGO hydrogel, HNP-RGO hydrogel, and Ba-HNP-RGO hydrogel, were then applied as scaffolds for neural engineering.

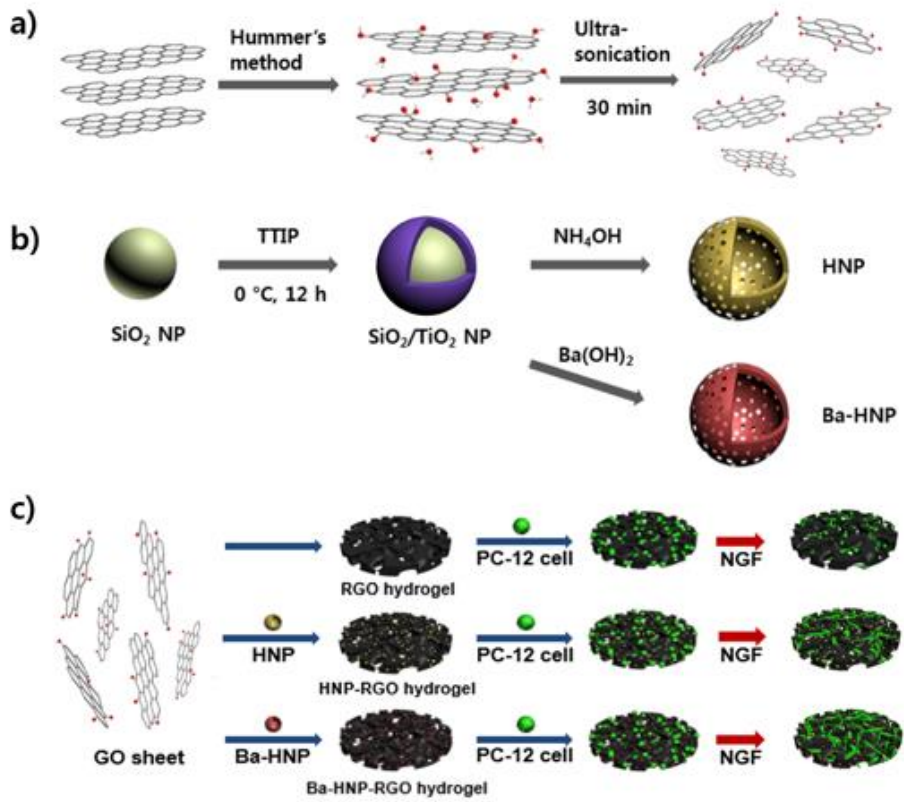


Figure 3. A schematic illustration describing the fabrication method of RGO hydrogels and their further application.

3.2 Characterization of RGO hydrogels

3.2.1 Morphology of RGO hydrogels

To prepare three types of graphene hydrogels, graphene oxide (GO) sheets and two types of hollow nanoparticles (HNPs) were used as building blocks. **Figure 4** displays TEM and AFM images of GO sheets and HNPs. Both TEM and AFM images shows that GO sheets had irregular shapes and a lateral dimension of up to 2 μm . Height-profile analysis (**inset of Figure 4b**) shows that the thickness of GO was *ca.* 3.285 nm corresponding to 5 layers. **Figure 4c** and **Figure 4d** demonstrates the well-defined hollow structure of HNP and Ba-HNP. The average diameter of particles was *ca.* 50 nm and the thickness of shell was *ca.* 5 nm. EDAX analysis (**Table 1**) indicates that HNP is composed of SiO_2 and TiO_2 in similar proportion and barium atoms were successfully introduced into silica/titania complex, making up almost 6.6 % of the Ba-HNP composition.

The physical appearance of graphene hydrogels is shown in **Figure 5**. Well mixed GO solution with or without HNPs turned into cylindrical hydrogels under hydrothermal treatment. RGO hydrogels were lyophilized after sufficient washing and then analyzed for physical and chemical characterizations. The morphology of the lyophilized RGO hydrogels was examined by SEM and mercury porosimetry. SEM images (**Figure 6**) of the lyophilized RGO

hydrogels clearly indicated the formation of 3D porous structure. GO sheets are cross-linked with one another through hydrogen bonding and π - π attraction as the reduction progresses, which leads to a 3D network like structure [46]. Higher magnification SEM images proves that the as-formed HNPs were homogeneously embedded in the hydrogels. As mentioned earlier, suitable pore size of scaffold is very important for cell injection and further cellular process. The pore size of hydrogels increased as the concentration of GO solution was reduced. Below the GO concentration of 0.5 mg mL^{-1} , GO sheets failed to form a self-supporting hydrogel because of low contact probability between GO sheets. In regard of the HNPs, they have negative charge so can act as repulsion improvers. Hence, addition of HNPs somewhat disturbed restacking of GO sheets. Therefore, the maximum amount of HNPs was experimentally counted as five times the amount of GO. The pore size of the RGO hydrogels fabricated at the conditions (the mass ratio of GO: HNPs: VC is 1: 5: 10 and C_{GO} is 0.5 mg mL^{-1}) were measured approximately from SEM images (**Figure 6a, b and c**) and the pore size distribution was achieved by Mercury porosimetry analysis (**Figure 7**). It was clearly observed from the SEM images that pores are large enough for PC12 cells to penetrate into RGO hydrogels. The mean pore size of the RGO gels determined by mercury porosimetry was $6.71 \text{ }\mu\text{m}$, $5.94 \text{ }\mu\text{m}$ and $10.08 \text{ }\mu\text{m}$, respectively. These results are in the range of PC12 cell size and the existence of pores $> \sim 10 \text{ }\mu\text{m}$ enables cells to get into the hydrogels easily and further provides efficient paths for delivery of nutrients and wastes. The

appearance of the size distribution graph was highly fluctuated in the case of HNPs used RGO-hydrogels. The diversity of pore size resulted from the decrease of lateral dimension of GO sheets. At low pH, oxygen containing groups of GO were protonated, and the positive fields around OH-groups increased. HNPs with negative charge adhered to GO surface through interaction with positive fields, and then some of HNPs were encapsulated by GO sheets, which reduced the size of GO sheets. Contrary to $\text{SiO}_2/\text{TiO}_2$, barium ion is one of divalent ions promoting GO gelation through coordination with hydroxyl and carboxyl groups on GO sheets. Collectively, the combination of the effects of HNP and Ba was estimated to lead to more larger and uniform size of pores in Ba-HNP-RGO hydrogels than HNP-RGO hydrogels.

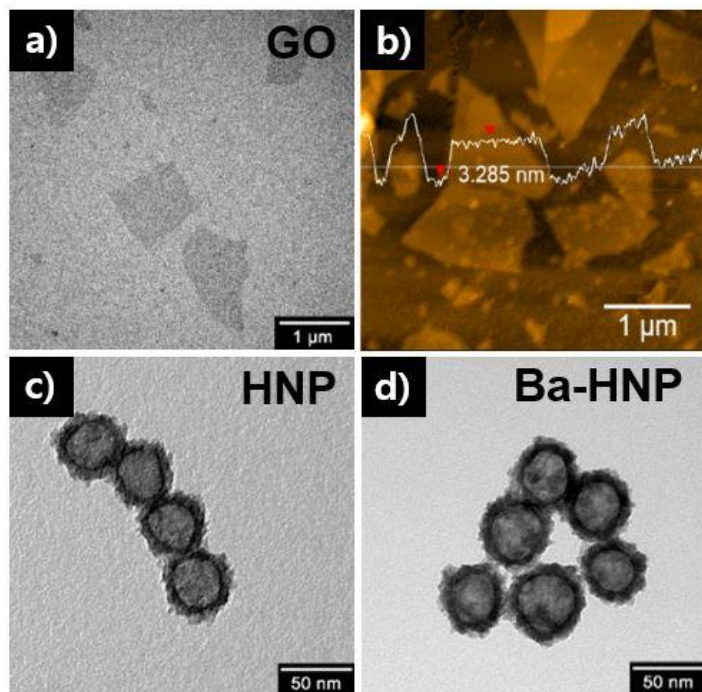


Figure 4. TEM images of a) GO, c) HNPs and d) Ba-HNPs. b) AFM image of GO (the inset shows the height profile along the line).

Table 1. Elemental Analysis of HNP and Ba-HNP

Materials	Atomic %				
	Si	Ti	O	Ba	Total
HNP (SiO ₂ /TiO ₂)	11.63	13.83	74.54	–	100.0
Ba-HNP (Ba-SiO ₂ /TiO ₂)	9.57	10.36	73.50	6.57	100.0

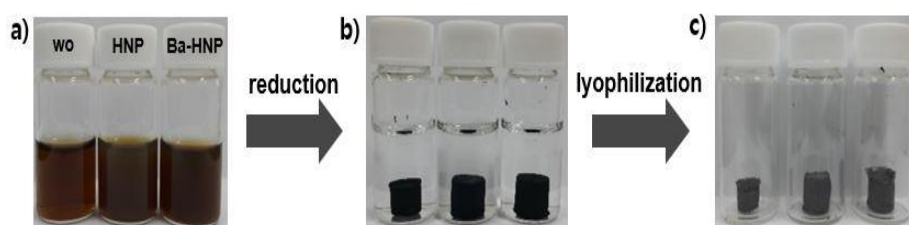


Figure 5. Photographs of a) GO mixtures, b) hydrogels and c) lyophilized gels.

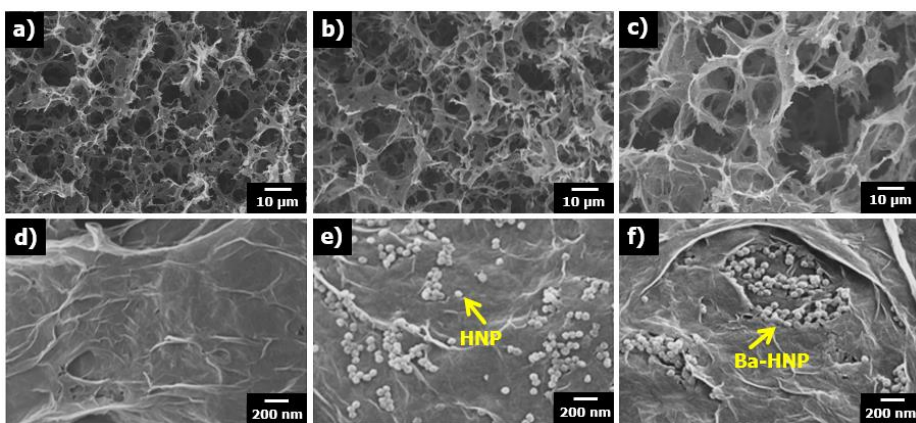


Figure 6. a-c) Low-magnification and d-f) high-magnification SEM images of RGO, HNP-RGO and Ba-HNP-RGO aerogels, respectively.

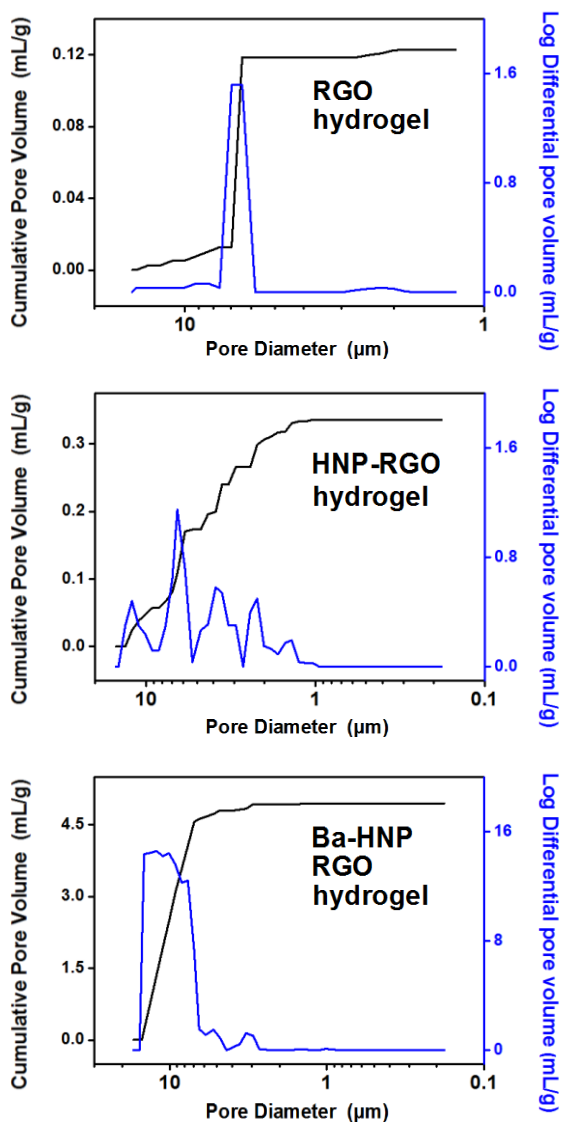


Figure 7. Pore size distribution of the three hydrogels by mercury porosimetry intrusion analysis.

3.2.2 Characterization of RGO hydrogels

To determine the stiffness of the three RGO hydrogels, rheological analysis was conducted using a TA instrument AR-G2 rheometer with a parallel-plate geometry. Elastic modulus were acquired under a frequency sweep mood in the linear viscoelastic region (1–100 Hz) with a fixed stress, which was obtained from stress sweep tests. **Figure 8** shows the results of the frequency sweep tests. The obtained modulus was in the order of RGO hydrogel > Ba-HNP-RGO hydrogel > HNP-RGO hydrogel. Notably, the modulus of the hydrogels with HNPs was lower than raw RGO hydrogel, which could be attributed to the decrease of lateral dimension of GO sheets. On the contrary, the coordination effect of barium ion significantly increased the modulus of the Ba-HNP-RGO hydrogel by aiding crosslinking. All the measured values were within the scope of modulus for PC12 cell culture and neural tissues (10^2 – 10^4 Pa) including spinal cord and gray matter.

Chemical properties of hydrogels are experimented by XPS and FT-IR analyses. The reduction of GO was also confirmed by those analyses. As shown in **Figure 9**, deconvoluted C1s spectra of GO and the RGO hydrogels have five peaks at 284.5, 285.6, 286.6, 288.0 and 289.2 eV, which corresponds to sp^2 carbon, sp^3 carbon, hydroxyl or epoxy group, carbonyl group and carboxyl group, respectively. After hydrothermal reduction, the peak intensity of oxygen containing groups decreased but that of the sp^2 carbon increased owing to

recovery of sp^2 carbon structure. The C/O ratio obtained from XPS data was 2.40 (GO), 4.50 (RGO), 3.5 (HNP-RGO), 3.07 (Ba-HNP-RGO), which meant that GO was moderately reduced under mild reduction condition. The residue of oxygen containing groups and regenerated sp^2 carbon domains could assist the adsorption of cells and nutrients as mentioned previously. The functional groups on the surface of the three hydrogels were further confirmed by FT-IR analysis. **Figure 10** exhibits FT-IR spectra of GO film and the three RGO hydrogels. Several oxygen-related peaks were observed in all the FT-IR spectra. The broad peak centered at 3200 cm^{-1} was attributed to the O-H stretching of hydroxyl group and the peaks at 1730 cm^{-1} was assigned to the C=O vibration of carbonyl group. Additional peak at 1032 cm^{-1} was designated for the C–O stretching vibrations. The peak due to the O-H deformation appeared at 1397 cm^{-1} . The peak at 1615 cm^{-1} was attributed to the skeletal vibrations of unoxidized graphitic domains. The intensity of oxygen-related peaks were diminished in the spectra of the three hydrogels compared with GO owing to the cleavage of oxygen-containing groups.

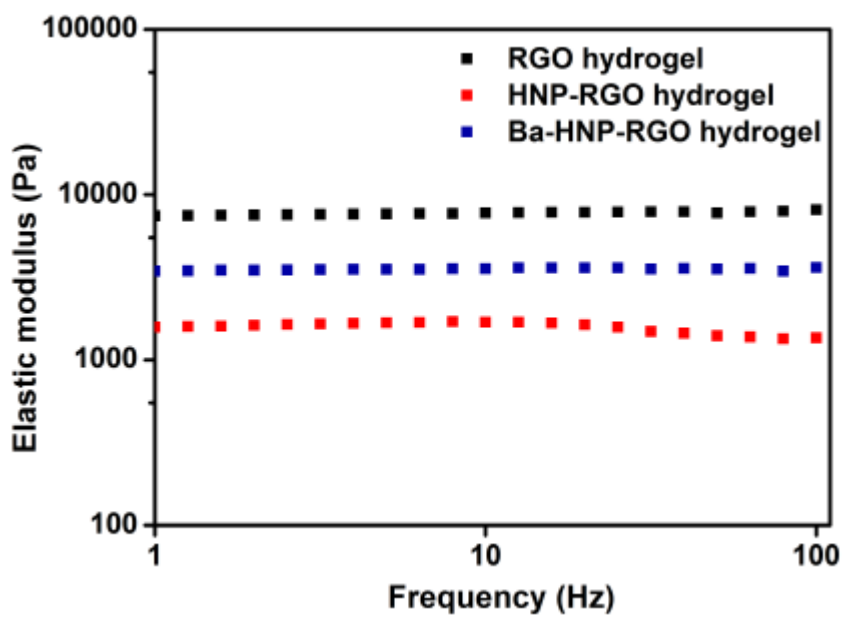


Figure 8. Elastic modulus of different hydrogels during frequency sweep analysis.

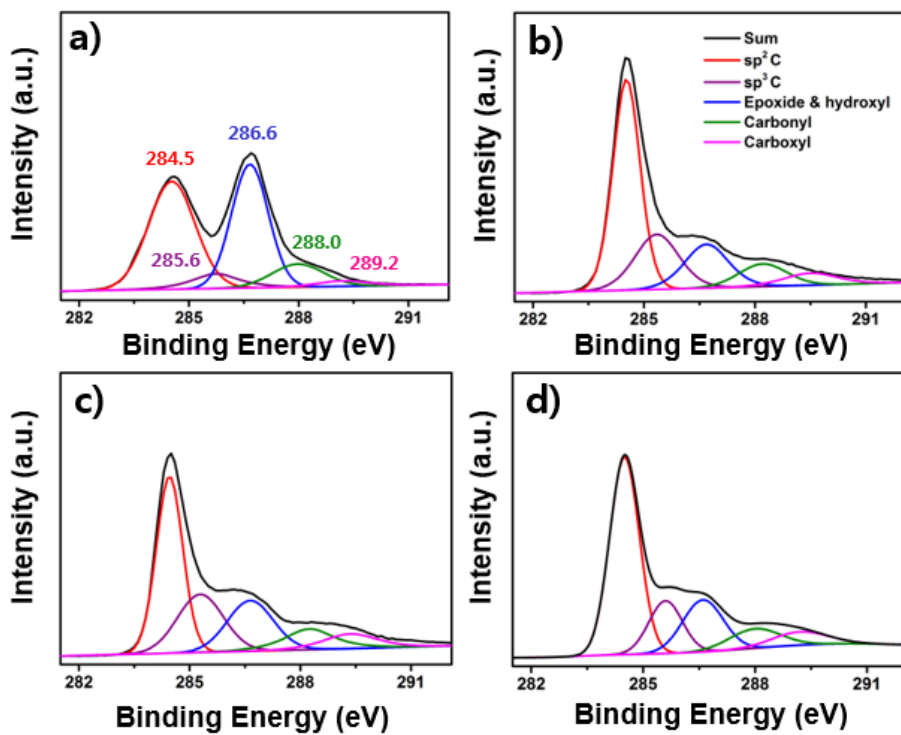


Figure 9. High resolution C1s XPS spectra of a) GO film, b) RGO, c) HNP-RGO and d) Ba-HNP-RGO aerogels.

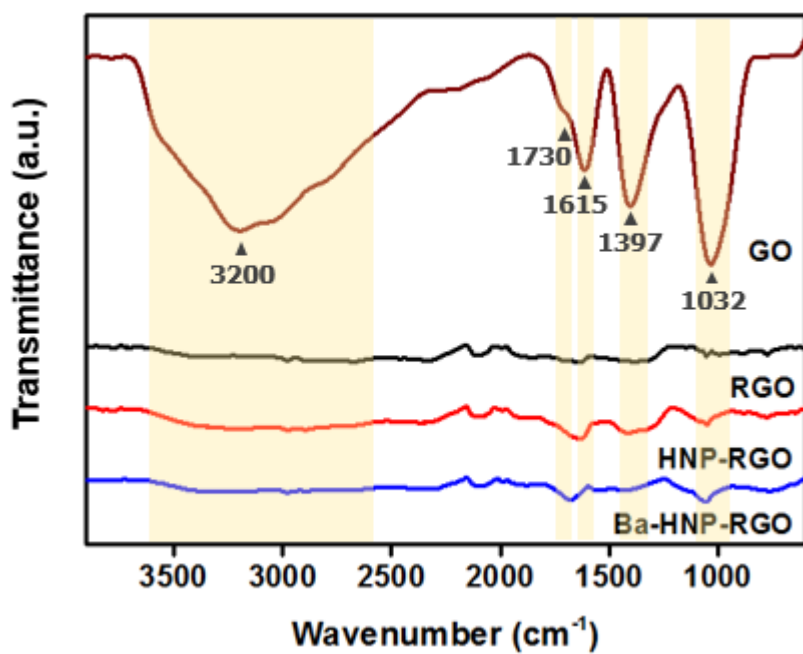


Figure 10. FT-IR spectra of GO and lyophilized RGO hydrogels showing the removal of oxygen containing groups from GO.

3.3 Application as scaffolds for neurons

3.3.1 Cell viability and proliferation

Prior to the application of a scaffold for cell culture, the biocompatibility of the three hydrogels should be assessed. PC12 cells known to have neurogenic differentiation potency were chosen for *in vitro* studies. First, the ATP contents which are proportional to the number of cells were measured for 3 days (**Figure 11a**). As a negative control experiment, the PC12 cells were cultivated onto the cover slip glass without any NGF or hydrogel treatment. The amount of ATP measured was in order of HNP-RGO hydrogel > Ba-HNP-RGO hydrogel > RGO hydrogel > Glass all through Day 1–3. This result was correlated with the modulus of hydrogels analysed above. In addition, the proliferation rate was calculated using an equation as following:

$$\text{proliferation rate} = \frac{\text{ATP amount}_{\text{Day } n+1} - \text{ATP amount}_{\text{Day } n}}{\text{ATP amount}_{\text{Day } n}} \times 100 (\%) \quad (1)$$

From this calculation, **Figure 11b** indicated that the number of cells on the glass dramatically increased at Day1 to Day 2. This result was interpreted as not the proliferation of cells attached on glass but the additional attachment of floating cells which failed to adhere to the glass for 24 hours after seeding. Therefore, the value of Day 2 to Day 3 was the authentic proliferation rate for the cells seeded on the glass. The proliferation rate on the three hydrogels was 170 % (Day 1 to Day 2), 270 % (Day 2 to Day 3) on average, which was higher

than that on the glass. These data demonstrated that the three hydrogels facilitated proliferation of PC12 cells more than the glass, but there was no significant difference in cell proliferative ability between the three hydrogels. Judging from these results, we concluded that the tendency from **Figure 11a** was attributed to the amount of attached cells for 24 hours after seeding. Furthermore, it could be confirmed that the attachment of cells was affected by the scaffold stiffness.

Reactive oxygen species (ROS) such as peroxides, singlet oxygen and hydroxyl radical are continuously generated during metabolic processes. However, excess ROS can lead to oxidative damage to DNA, lipids and proteins. Thus, reactive oxygen species (ROS) generation assay was also conducted to verify the biocompatibility of hydrogels. In this assay, we used two controls; one was a negative control (cells grew on the glass) and the other was a positive control (cells on the glass were treated with H₂O₂). **Figure 11c** shows the relative amount of ROS generation with respect of positive control (100%). The percentages of ROS on the three hydrogels were below 20 % even incubated for 3 days. This result indicated low-cell toxicity of the RGO hydrogels, which was also supported by Live/dead cell double staining images. In **figure 12**, live cells appeared fluorescent green and dead cells were stained red. There was no noteworthy difference between the cells seeded on glass and on the hydrogels. Nevertheless, the ROS levels of the cells seeded on the three hydrogels were comparably higher than negative control. As moderate ROS

revel provides a beneficial effect on cell metabolism and protein translation, it was thought that the difference of cell activities observed in this work could be associated with the ROS generation amount per cell. Thus, the value of ROS amount per cell was obtained by dividing the ROS amount by ATP amount. It was remarkable that the ROS level per cell was in order of Ba-HNP-RGO hydrogel > HNP-RGO hydrogel > RGO hydrogel > Glass (negative control), which was coincided with the result of cell differentiation analysis (discussed in the next section).

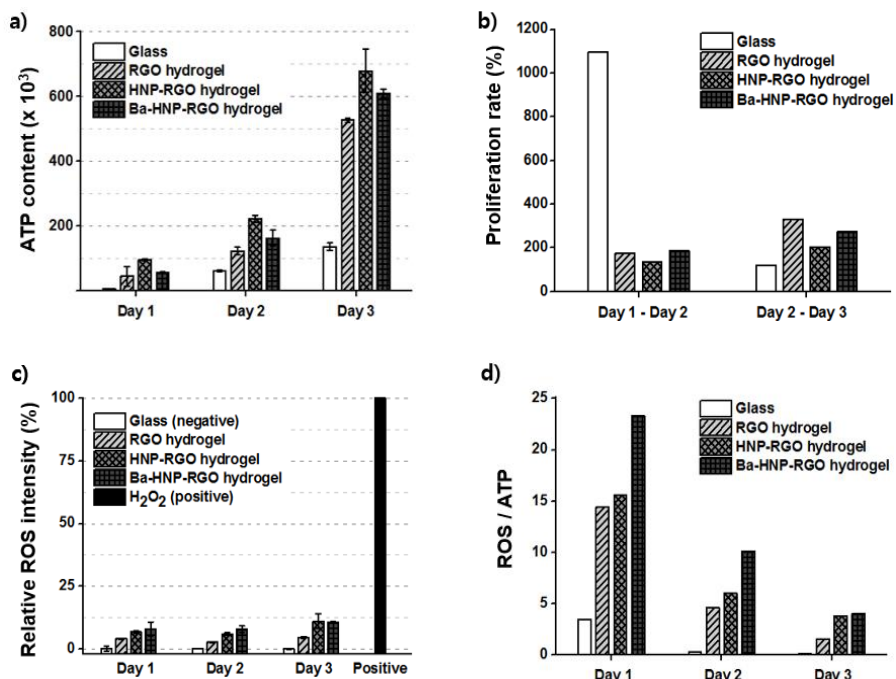


Figure 11. a) ATP content of, b) Proliferation rate of, c) ROS production of, d) ROS intensity divided ATP content of the PC12 cells incubated on glass and different sort of hydrogels. The experiments were conducted with time dependence (1–3d). Values exhibit mean \pm SD and independent experiments were performed three times ($n = 3$). H_2O_2 was taken as a positive control for ROS production.

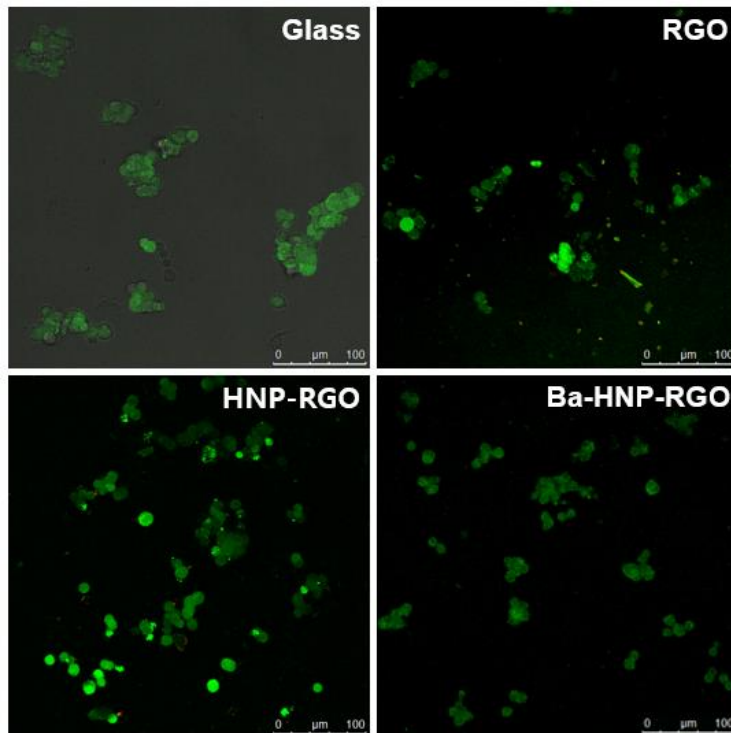


Figure 12. Live and dead PC 12 cells on different scaffolds. Live cells (green) were stained with a cell-permeant calcein AM, and dead cells (red) were marked with a cell-impermeant dye.

3.3.2 Cell differentiation

During cell differentiation process, PC12 cells express the beta-tubulin (III), a neuron-specific microtubule element. To estimate neuronal growth on the three hydrogels, the cells were cultured on glass (control experiment) and three hydrogels. The microtubules grown from 3D scaffold, were visualized by immunofluorescence beta-tubulin antibodies. As shown in **Figure 13**, PC12 cells grown on glass developed a number of short neurites. In contrast, PC12 cells grown on the three hydrogels had longer and thicker neurites. Average length of total branching tree and the longest neurite and average number of primary neurites and branching points per primary neurites were calculated from the immunofluorescent images (**Figure 14**). The average length of total branching tree was in order of Ba-HNP-RGO hydrogel > HNP-RGO hydrogel > RGO hydrogel > Glass. The average length of the longest neurites had a similar trend. Notably, the number of neurites originating from cell body was higher in the cells cultured on glass than in the cells cultured on the hydrogels, whereas the number of branching sites was the reverse. These results indicates that RGO based hydrogels facilitated the elongation and branching of primary neurite rather than formation of new neurites and the HNPs assisted the elongation in the order of Ba-HNP > HNP.

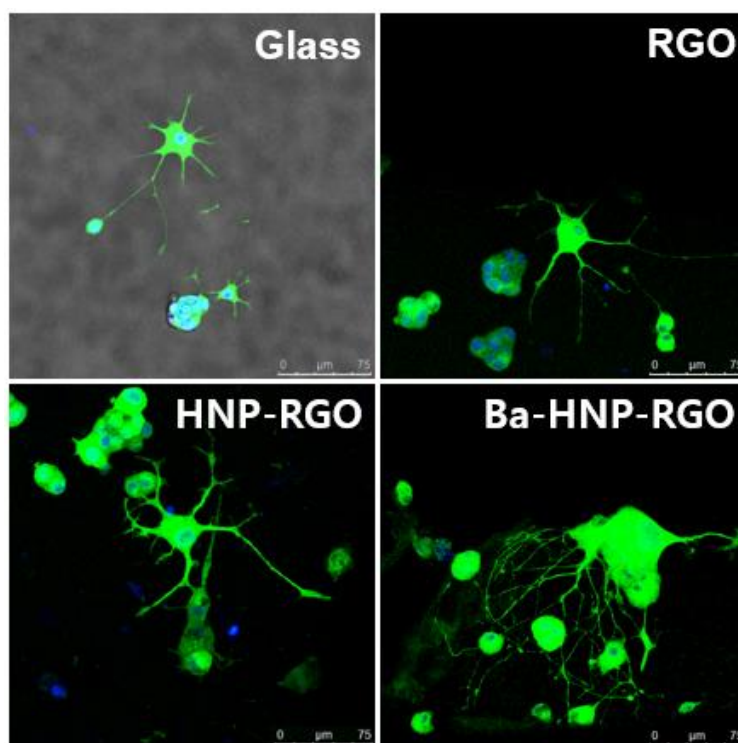


Figure 13. Immunofluorescent images of the PC12 cells incubated on different sort of hydrogels. The differentiated PC12 cells were stained with β -tubulin (class III; neural specific marker; green) and DAPI (nucleus; blue).

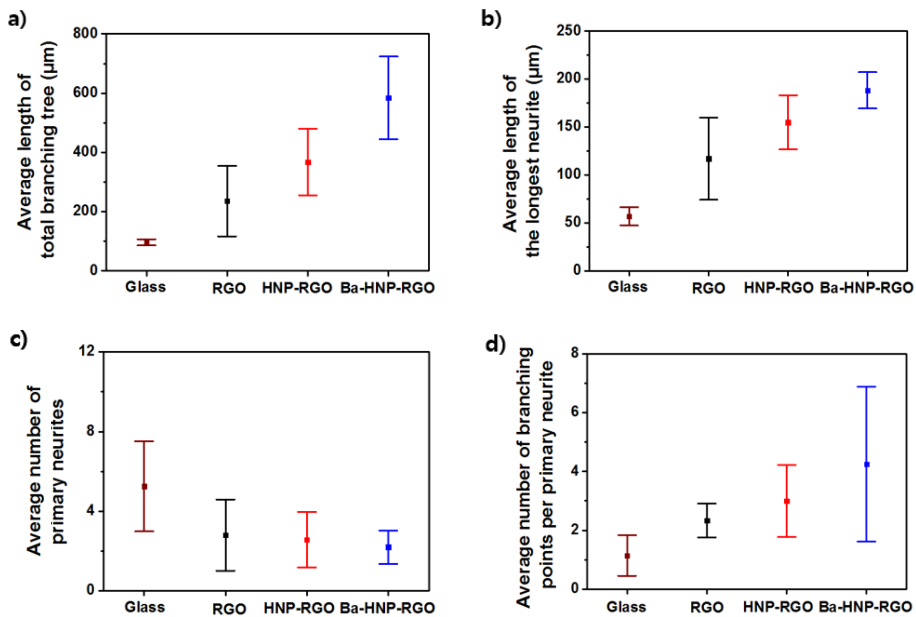


Figure 14. Morphological analyses of PC12 cell growth on glass and different sort of hydrogels. Average length of a) total branching tree and b) the longest neurite and average number of c) primary neurites and d) branching points per primary neurite.

3.3.3 The signal transduction pathways

The neuronal growth enhancement was in order of Ba-HNP-RGO hydrogel > HNP-RGO hydrogel > RGO hydrogel > Glass, which was similar result with the ROS level of cells. In general, ROS has an important role in the neuronal differentiation as a messenger molecule. In particular, oxidative stress like ROS can activate the MAPK pathways through oxidative protein modification such as phosphorylation. Therefore, the expression levels of phosphorylated MAPKs including pERK, pJNK, pp38 and TrkA receptor for NGF were measured to explore how neurons were affected by the three hydrogels (**Figure 15**). TrkA, one of receptors on cell membrane, is activated by binding with NGF. Comparing with cells grown on glass, the expression level of TrkA was not substantially increased at the cells grown on the three hydrogels. This result implied that delivery of NGF to cells was not disturbed by the porous structure of hydrogels. The phosphorylation of ERK protein was not affected by RGO but facilitated by the HNPs in order of Ba-HNP > HNP. In the case of p38 protein under the highly sensitive pathway to stress, the expression level of pp38 was dramatically increased as following order: Ba-HNP-RGO hydrogel > HNP-RGO hydrogel > RGO hydrogel > Glass. pJNK proteins were more expressed in the cells on the three hydrogels than in the cells on glass without regard to existence of the HNPs. Thanks to substantial activation of JNK, which is critical for cell survival during differentiation by controlling cell cycle and

retarding apoptosis, there was no significant cell death even in more active cells under impetus from the three RGO hydrogels.

Collectively, the stimulus from RGO material improved neuronal growth and cell survival during differentiation through p38 and JNK pathways. Moreover, the cellular stress from HNP and Ba-HNP accelerated ERK and p38 pathways. Additional expression of pERK and pp38 from barium ions was thought to be due to the activation of calcium related pathways because several alkaline earth metals could pass through the calcium ion channel and act like calcium ions [47].

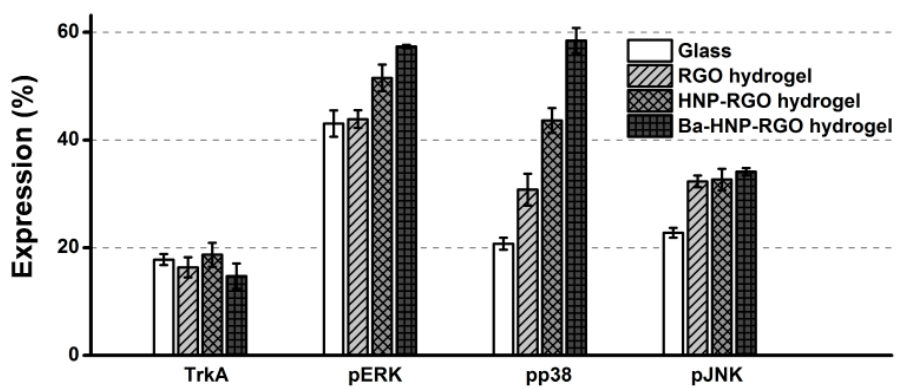


Figure 11. The activation of MAPK pathway-related proteins of PC12 cells cultured on glass an different hydrogels for day 3.

Chapter 4. Conclusion

In this work, three types of RGO based hydrogels were successfully fabricated with proper pore size and scaffold stiffness for PC12 cells. All the hydrogels were highly biocompatible and enhanced both cell proliferation and differentiation. Regardless of nanoparticle insertion, the proliferation rate was slightly higher on the three hydrogels than on glass. Furthermore, neuronal outgrowth was drastically improved on the three hydrogels in order of Ba-HNP-RGO hydrogel > HNP-RGO hydrogel > RGO hydrogel by activating MAPK pathways. Specifically, RGO supported cell differentiation and survival through activating p38 and JNK pathways, and the HNPs further facilitated neuronal growth through activating ERK and p38 pathways. To the best of our knowledge, this is the first study investigating how RGO hydrogel affects activities of neurons through MAPK pathways. This study showed the possibility of RGO based hydrogels as scaffolds for neuronal tissue engineering and explored one of possible neural signaling pathways of the RGO hydrogel for further research.

References

- [1] D. J. Mooney, A. G. Mikos, *Scientific American*, **1999**.
- [2] S. Yang, K.-F. Leong, Z. Du, C.-K. Chua, *Tissue engineering*, **2001**, 7, 679
- [3] T. Dvir, B. P. Timko, D. S. Kohane, R. Langer, *Nature nanotechnology*, **2011**, 6, 13.
- [4] L. G. Griffith, G. Naughton, *Science*, **2002**, 295, 1009.
- [5] M. Tsintou, K. Dalamagkas, A. M. Seifalian, *Neural. Regen. Res.*, **2015**, 10, 726.
- [6] R. Cancedda, B. Dozin, P. Giannoni, R. Quarto, *Matrix Biology*, **2003**, 22, 81.
- [7] W. J. Zhang, W. Liu, L. Cui, Y. Cao, *Journal of cellular and molecular medicine*, **2007**, 11, 945.
- [8] J. W. Allen, S. N. Bhatia, *Tissue engineering*, **2002**, 8, 725.
- [9] L. Ma, C. Gao, Z. Mao, J. Zhou, J. Shen, X. Hu, C. Han, *Biomaterials*, **2003**, 24, 4833.
- [10] S. Levenberg, J. Rouwkema, M. Macdonald, E. S. Garfein, D. S. Kohane, D. C. Darland, R. Marini, C. A. van Blitterswijk, R. C. Mulligan, P. A. D'Amore, *Nature biotechnology*, **2005**, 23, 879.
- [11] C. E. Schmidt, J. B. Leach, *Annual review of biomedical engineering*, **2003**, 5, 293.
- [12] K. Whang, K. Healy, D. Elenz, E. Nam, D. Tsai, C. Thomas, G. Nuber, F.

- Glorieux, R. Travers, S. Sprague, *Tissue engineering*, **1999**, 5, 35.
- [13] S.-M. Lien, L.-Y. Ko, T.-J. Huang, *Acta Biomaterialia*, **2009**, 5, 670.
- [14] V. Melissinaki, A. Gill, I. Ortega, M. Vamvakaki, A. Ranella, J. Haycock, C. Fotakis, M. Farsari, F. Claeysens, *Biofabrication*, **2011**, 3, 045005.
- [15] N. E. Zander, J. A. Orlicki, A. M. Rawlett, T. P. Beebe Jr, *Journal of Materials Science: Materials in Medicine*, **2013**, 24, 179.
- [16] A. J. Engler, S. Sen, H. L. Sweeney, D. E. Discher, *Cell*, **2006**, 126, 677.
- [17] P. C. Georges, W. J. Miller, D. F. Meaney, E. S. Sawyer, P. A. Janmey, *Biophysical journal*, **2006**, 90, 3012.
- [18] M. Buttiglione, F. Vitiello, E. Sardella, L. Petrone, M. Nardulli, P. Favia, R. d'Agostino, R. Gristina, *Biomaterials*, **2007**, 28, 2932.
- [19] E. V. Romanova, S. P. Oxley, S. S. Rubakhin, P. W. Bohn, J. V. Sweedler, *Biomaterials*, **2006**, 27, 1665.
- [20] G. Wu, J. Wang, X. Chen, Y. Wang, *Journal of Biomedical Materials Research Part A*, **2014**, 102, 3439.
- [21] T.-H. Young, H.-H. Chang, D.-J. Lin, L.-P. Cheng, *Journal of Membrane Science*, **2010**, 350, 32.
- [22] W. Zhang, H. T. Liu, *Cell research*, **2002**, 12, 9.
- [23] L. Klesse, K. Meyers, C. Marshall, L. Parada, *Oncogene*, **1999**, 18.
- [24] E. T. Coffey, *Nature Reviews Neuroscience*, **2014**, 15, 285.
- [25] R. Hayakawa, T. Hayakawa, K. Takeda, H. Ichijo, *Proceedings of the Japan Academy, Series B*, **2012**, 88, 434.

- [26] K. Takeda, H. Ichijo, *Genes to Cells*, **2002**, 7, 1099.
- [27] D. Chuderland, R. Seger, *Communicative & integrative biology*, 2008, 1, 4.
- [28] M. D. Stoller, S. Park, Y. Zhu, J. An, R. S. Ruoff, *Nano letters*, **2008**, 8, 3498.
- [29] C. Lee, X. Wei, J. W. Kysar, J. Hone, *science*, **2008**, 321, 385.
- [30] H. He, J. Klinowski, M. Forster, A. Lerf, *Chemical physics letters*, **1998**, 287, 53.
- [31] V. Georgakilas, M. Otyepka, A. B. Bourlinos, V. Chandra, N. Kim, K. C. Kemp, P. Hobza, R. Zboril, K. S. Kim, *Chemical reviews*, **2012**, 112, 6156.
- [32] N. Li, Y. Cheng, Q. Song, Z. Jiang, M. Tang, G. Cheng, *Chin. Sci. Bull.* **2014**, 59, 1341.
- [33] S. K. Lee, H. Kim, B. S. Shim, *Carbon letters*, **2013**, 14, 63.
- [34] C. Shuai, P. Feng, C. Gao, X. Shuai, T. Xiao, S. Peng, *RSC Adv.*, **2015**, 5, 25416.
- [35] S. Kang, J. B. Park, T.-J. Lee, S. Ryu, S. H. Bhang, W.-G. La, M.-K. Noh, B. H. Hong, B.-S. Kim, *Carbon*, **2015**, 83, 162.
- [36] P.-P. Zuo, H.-F. Feng, Z.-Z. Xu, L.-F. Zhang, Y.-L. Zhang, W. Xia, W.-Q. Zhang, *Chemistry Central Journal*, **2013**, 7, 1.
- [37] W. C. Lee, C. H. Y. Lim, H. Shi, L. A. Tang, Y. Wang, C. T. Lim, K. P. Loh, *ACS nano*, **2011**, 5, 7334.
- [38] H. Chen, M. B. Müller, K. J. Gilmore, G. G. Wallace, D. Li, *Advanced*

- Materials*, **2008**, 20, 3557.
- [39] N. Li, Q. Zhang, S. Gao, Q. Song, R. Huang, L. Wang, L. Liu, J. Dai, M. Tang, G. Cheng, *Scientific reports*, **2013**, 3.
- [40] O. Akhavan, *J. Mater. Chem. B*, **2016**, 4, 3169.
- [41] N. Li, X. Zhang, Q. Song, R. Su, Q. Zhang, T. Kong, L. Liu, G. Jin, M. Tang, G. Cheng, *Biomaterials*, **2011**, 32, 9374.
- [42] S. Shah, P. T. Yin, T. M. Uehara, S. T. D. Chueng, L. Yang, K. B. Lee, *Advanced materials*, **2014**, 26, 3673.
- [43] Z. Sui, X. Zhang, Y. Lei, Y. Luo, *Carbon*, **2011**, 49, 4314.
- [44] W. H. Suh, A. R. Jang, Y. H. Suh, K. S. Suslick, *Advanced Materials*, **2006**, 18, 1832.
- [45] M. Choi, C. Kim, S. O. Jeon, K. S. Yook, J. Y. Lee, J. Jang, *Chemical Communications*, **2011**, 47, 7092.
- [46] D. R. Dreyer, S. Park, C. W. Bielawski, R. S. Ruoff, *Chemical Society Reviews*, **2010**, 39, 228.
- [47] T. Curran, J. I. Morgan, *Proceedings of the National Academy of Sciences*, **1986**, 83, 8521.

초 록

조직공학은 세포와 지지체, 세포활성을 조절할 수 있는 인자들의 복합체로 인체의 손상된 조직이나 기관을 회복시키거나 대체하는 기술로서 많은 관심을 받아왔다. 인공 조직의 임상적인 응용을 위해서는 세포가 부착하고 분화하여 새로운 조직을 형성할 수 있도록 삼차원의 구조물이 제공되어야 하며 동시에 지지체 자체가 적절한 자극을 제공할 수 있어야 한다. 환원그래핀 하이드로겔은 다공성의 삼차원의 구조로 제조가 용이하며 표면의 작용기는 세포에 자극을 제공할 수 있다. 특히나 그래핀은 전도성 물질로서 추가적인 전기자극을 세포에 부여할 수 있어 신경조직의 지지체로 유용할 것이라 판단된다. 하지만 그래핀 기반의 지지체 중 신경조직과 강성이 유사한 환원그래핀 하이드로겔의 지지체로의 연구는 미비한 실정이다. 또한 이와 같은 물질이 어떻게 신경세포의 신호전달 기작에 관여하는지에 대한 기초적인 연구가 부족하다. 본 논문에서는, 세포활성의 나노입자가 도입된 삼차원 다공성 구조의 환원그래핀 하이드로겔을 제조하여 이를 신경세포의 지지체로 적용하였다. 흑연의 화학적 산화방법으로 제조한 산화그래핀을 아스코르브산을 이용해 환원시켜 삼차원의 환원그래핀 하이드로겔을 제조하였고 나노입자를 혼합한 산화그래핀 용액으로부터

나노입자가 도입된 하이드로겔을 제조하였다. 제조된 하이드로겔은 신경조직에 적절한 기공과 강성을 가짐을 확인하였으며 신경세포의 지지체로 적용하였을 때 우수한 생체적합성과 생체활성을 보였다. 또한 신경세포 분화과정에서, 환원그래핀의 경우 p38과 JNK 신호전달계의 활성을 촉진하고 도입한 나노입자는 ERK와 p38 신호전달계의 활성을 촉진시킨 것을 확인할 수 있었다. 이 논문은 환원그래핀 기반의 하이드로겔의 신경세포의 지지체로 응용 가능성을 제시하며 환원그래핀의 신호전달 기작으로의 영향에 대한 이해를 도울 것으로 사료된다.

주요어 : 조직공학, 환원그래핀 하이드로겔, 나노입자, PC12 세포, 세포분화, 신호전달 기작.

학번 : 2015-21026